



**HAL**  
open science

## Investigation of salt precipitation dynamic in porous media by X-ray and Neutron dual-modality imaging

Matthieu Mascle, Olivier Lopez, Herve Deschamps, Lars Rennan, Nicolas Lenoir, Alessandro Tengattini, Souhail Youssef

► **To cite this version:**

Matthieu Mascle, Olivier Lopez, Herve Deschamps, Lars Rennan, Nicolas Lenoir, et al.. Investigation of salt precipitation dynamic in porous media by X-ray and Neutron dual-modality imaging. Science and Technology for Energy Transition, 2023, 78, pp.11. 10.2516/stet/2023009 . hal-04106755

**HAL Id: hal-04106755**

**<https://ifp.hal.science/hal-04106755>**

Submitted on 25 May 2023

**HAL** is a multi-disciplinary open access archive for the deposit and dissemination of scientific research documents, whether they are published or not. The documents may come from teaching and research institutions in France or abroad, or from public or private research centers.

L'archive ouverte pluridisciplinaire **HAL**, est destinée au dépôt et à la diffusion de documents scientifiques de niveau recherche, publiés ou non, émanant des établissements d'enseignement et de recherche français ou étrangers, des laboratoires publics ou privés.



Distributed under a Creative Commons Attribution 4.0 International License

# Investigation of salt precipitation dynamic in porous media by X-ray and Neutron dual-modality imaging

Matthieu Mascle<sup>1,\*</sup> , Olivier Lopez<sup>2</sup>, Herve Deschamps<sup>1</sup>, Lars Rennan<sup>2</sup>, Nicolas Lenoir<sup>3,4</sup>, Alessandro Tengattini<sup>3,4</sup>, and Souhail Youssef<sup>1</sup>

<sup>1</sup> IFP Energies Nouvelles, 1 et 4 avenue de Bois Préau, 92852 Rueil-Malmaison, France

<sup>2</sup> Equinor ASA, Arkitekt Ebbells veg 10, 7053 Ranheim, Norway

<sup>3</sup> Univ. Grenoble Alpes, Grenoble INP, 46 Avenue Felix Viallet, 38031 Grenoble, France

<sup>4</sup> Institut Laue-Langevin (ILL), 71 Avenue des Martyrs, 38000 Grenoble, France

Received: 16 January 2023 / Accepted: 22 March 2023

**Abstract.** In this work, a new dual modality monitoring technique is presented to demonstrate its interest to investigate the salt precipitation dynamics induced by gas flow-through drying. It consists of imaging simultaneously a core flood using both Neutron and X-ray beams. A method to calibrate and process the two signals is presented. It takes advantage of the difference in attenuation between the two ionizing radiations to quantify the different phase saturations and compositions as well as the reduction of porosity caused by salt precipitation. A set of experiments has been conducted at the NeXT-Grenoble beamline of the *Institute Laue-Langevin* facilities (ILL, France). Experiments were conducted on a homogeneous rock sample of Bentheimer sandstone using dry nitrogen and a 100 g/L KBr brine. The two first experiments aimed to calibrate the dual modality for the different phases. The last two experiments have been conducted with a brine capillary contact maintained at the gas outlet. Experimental data have given new insights into the organization of the three phases (the brine, the gas, and the precipitated salt) when a salt bank is formed in the sample. These quantities computed using dual-modality imaging show great similarities with published work. The salt accumulation was used to estimate the flow rate of brine pumped through the capillary contact to compensate for the brine evaporation in the gas phase. Observations have shown that a reduction of the initial porosity in some sections of the sample by 12–14% was enough to trigger a gas draw-down characterized by the migration of the salt toward the gas inlet. In some conditions (low gas inlet pressure for example), the rise of the water could be fast enough to form a second salt bank higher in the sample. It has been observed that the formation of the second salt bank could spread the precipitated salt in a less damaging configuration for the gas flow, triggering a phase of gas build-up characterized by the withdrawal of the water. These phases of gas draw-down and build-up could alternate until the sample clogs.

**Keywords:** Salt precipitation, Neutron monitoring, X-ray monitoring, Drying, Dual modality.

## 1 Introduction

The injection of a dry gas phase through a water-saturated porous medium can reduce the saturation above the residual water saturation ( $S_{wi}$ ) reached after a viscous displacement, by evaporation mechanisms. In the presence of brine, this process can induce salt crystallization and precipitation within the porous medium. This phenomenon has been reported at the field scale [1], causing a substantial decline in good injectivity. Salt precipitation has been investigated in many studies, theoretically [2, 3], experimentally [4–7] and numerically [2, 8–12]. These studies aimed to understand the physical and chemical interplay between

the gas injection, capillary forces, and the porous structure. They distinguish two mechanisms of salt precipitation: the precipitation caused by the decrease of the gas pressure, leading to its expansion, and changing its equilibrium with the brine phase; and the precipitation caused by the injection of a dry gas in a partially saturated rock. The second mechanism is of interest here. They showed that the drying rate is proportional to the gas velocity and that any dissolved salt in the water can be transported by capillary flows induced by drying and can even accumulate near the injection surface. The permeability can then be reduced by pore clogging. They concluded that all these mechanisms must be included in models to calculate the near wellbore permeability and porosity changes with time, to correctly determine the good injectivity. Yet calibrating such a

\* Corresponding author: [matthieu.mascle@ifpen.fr](mailto:matthieu.mascle@ifpen.fr)

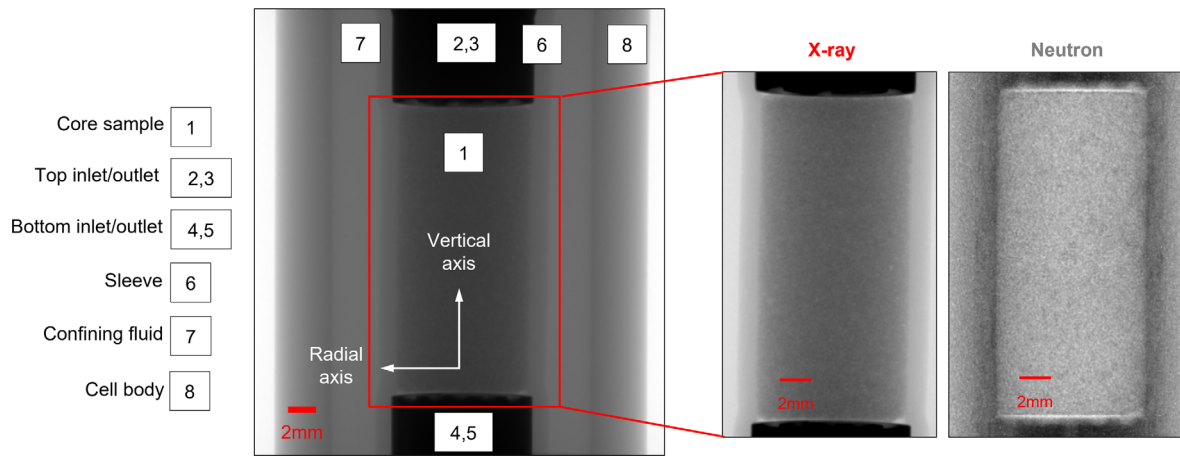


**Fig. 1.** Left: X-ray Radiography showing the Hassler injection cell. Right: X-ray and Neutron radiographies of the Bentheimer rock sample. X-ray and Neutron projections were acquired respectively at a pixel resolution of 40  $\mu\text{m}$  and 15  $\mu\text{m}$ .

multi-parameter model is not straightforward and requires advanced experimental investigation to properly quantify the key parameters such as local saturation and salt concentration as well as the porosity reduction or precipitated salt quantity [4, 13, 14].

In a previous study [4] a comprehensive experimental investigation of the effect of gas flow in a sandstone sample initially saturated with water or brine using X-ray radiography has been presented. This study has qualitatively shown the impact of brine capillary contact on the accumulation of salt within the sample during dry gas injection. Following Beer-Lambert law, X-ray intensity is attenuated by all crossed materials. The X-ray contrast is sensitive to all material variations including the water saturation and the salt concentration. X-ray monitoring is not capable by itself of de-correlate and quantifying the evolution of local water saturation, salt concentration and precipitate salt quantities (underdetermined system of equations).

To overcome this limitation, we adopted in this work a new *in-situ* monitoring instrument named NeXT-Grenoble and located at *Institute Laue-Langevin (ILL, France)* [15]. It allows for the simultaneous acquisition of both Neutron and X-ray radiographies. We took advantage of the difference in attenuation characteristics of Neutrons and X-rays [16, 17]. Indeed, while X-ray interacts with an atom's electron shell and is, therefore, more attenuated by material with higher atomic numbers, the neutron will mainly interact with atomic nuclei (if magnetic interaction is excluded). There is no straightforward relation between the Neutron attenuation coefficient and the atomic number, unlike X-rays. For example, Neutrons have a very high scattering cross section for hydrogen while chemical elements like Bromine (Br), which considerably attenuates X-ray, will be almost transparent to Neutrons. State-of-the-art equipment designed for *in-situ* core flood experimentation was used on NeXT-Grenoble to capture the dynamic of salt precipitation induced by gas flow-through drying. The experiments were conducted using a homogeneous rock sample of Bentheimer sandstone. First, the dry-out was conducted with deionized water to characterize the dynamic without salt precipitation. The same experiment was repeated with

KBr brine water to evaluate when salt precipitation occurred. Finally, the last experiment was conducted with the KBr brine, and a capillary contact was maintained at the core outlet. This experiment was repeated with two gas injection scenarios: a high and low gas pressure gradient.

The two first experiments aimed to establish and calibrate a method to compute the different phases from the Neutron and X-ray radiographies. The results of this calibration are given in the [Appendix](#). It was then applied to monitor the experiments conducted with the capillary contact. The dual-modality allowed for separately quantifying the dissolved and precipitated salt. Finally, the latter could be interpreted in terms of porosity reduction.

## 2 Materials and methods

### 2.1 Fluids and sample properties

Experiments have been conducted on a homogeneous Bentheimer sandstone of length and diameter  $L = 2.0$  cm and  $D = 9.32$  mm. The sample exhibited high porosity and permeability, measured to  $\phi = 23\%$  and  $K = 1500$  mD. Its pore volume was measured to  $PV = 0.31$  cc. X-ray and Neutron radiographies of the sample are shown in [Figure 1](#) when saturated with nitrogen ( $\text{N}_2$ ).

Three different fluids have been used to perform the experiments: dry nitrogen  $\text{N}_2$  for the gas phase, deionized water for the first experiment and a 100 g/L KBr brine (this salt concentration is referred to as  $C_0$ ). KBr salt was used for its high electron density, giving a good X-ray contrast with the gas, as well as for its low Neutron attenuation. Experiments were conducted at ambient temperature ( $24 \text{ }^\circ\text{C} \pm 1 \text{ }^\circ\text{C}$ ). KBr solubility in deionized water was estimated to be 650 g/L in these conditions.

### 2.2 Experimental set-up

The experimental set-up used in this study is shown in [Figure 2](#). Nitrogen was injected from the top at a constant pressure using a downstream pressure regulator. The gas flow rate was monitored using a Coriolis mass flowmeter.

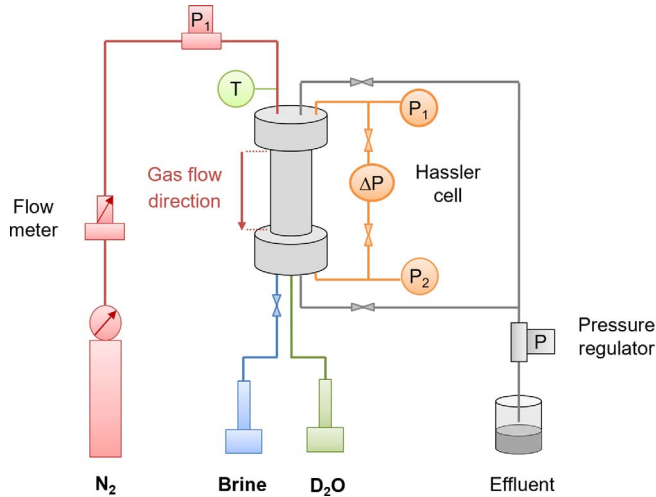


**Fig. 2.** Overview of the experimental set-up.

Brines (either deionized water or KBr brine) were injected using an ISCO-pump. The confining pressure was set to 10 bars using deuterated water ( $D_2O$ ) to be less attenuating to Neutrons compared to normal water ( $H_2O$ ), and a 1 mm thick perfluoro-elastomer (FFKM) sleeve. All tubings were connected to a Hassler-type cell. The main imaged components of the cell are presented in Figure 1. The cell was designed to bear more than 15 bars while being transparent to X-rays and Neutrons. The cell body was composed of a 2 mm thick Teflon cylinder, to mitigate both Neutron activation and attenuation. The cell was equipped from each side with three connections (inlet, outlet, and static line for the pressure transducer). The inlet/outlet pressures and differential pressure ( $dP$ ) were measured using a Keller differential pressure sensor. A data acquisition system was used to monitor the pressure, mass flow and temperature. Finally, the set-up was installed in dedicated radiography facility equipment for *in-situ* saturation monitoring.

For all dry-out tests, the sample was set vertically, with the gas injected from the top of the plug and the water from the bottom. The capillary contact (for experiments 3 and 4) is maintained by sweeping the bottom of the plug. For the 2D plots, the core axis was normalized as follows:  $x = 0$  referred to the bottom, and  $x = L$  refers to the top.

### 2.3 Experimental procedure

The four dry-out experiments were conducted using the same injection procedure:

1. Saturating the sample with the brine by injecting it from the bottom inlet and opening the top outlet (the bottom outlet and top inlet are closed). To ensure a full saturation, a back pressure of 7 bars was imposed after the water breakthrough to compress and produce the trapped gas.
2. Opening the bottom outlet and top inlet and closing the top outlet. The water injection was maintained to allow a sweeping of the bottom face of the sample.
3. After lowering the pore pressure to the atmosphere, the gas was injected at a constant pressure.

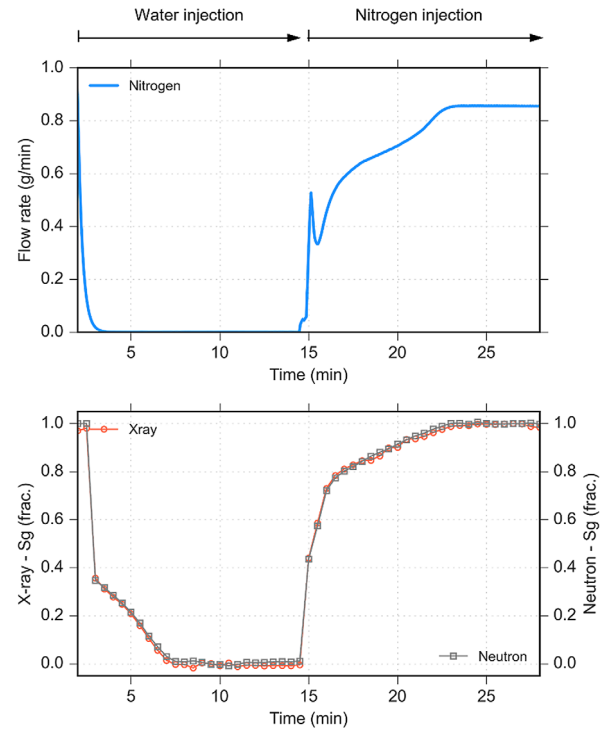


**Fig. 3.** Dry-out with deionized water. X-ray and Neutron beams are normalized between dry states and saturated with deionized water.

4. The sample was finally cleaned by injecting deionized water and increasing the back pressure until the X-ray attenuation stability was reached.

## 3 Results and discussion

The four tests are presented and interpreted hereafter. They have been conducted one after the other, in the same acquisition sequence, without interrupting the X-ray and Neutron beams. As mentioned in the introduction, the two first tests aimed at calibrating the dual modality monitoring method.

### 3.1 Dry out with the deionized water

Deionized water was used for this preliminary experiment. In these conditions, the Neutron and X-ray beams were expected to show the same trend when normalized between the dry and the saturated states. The Neutron and X-ray attenuations are plotted in Figure 3 with the mass flow rate. The protocol described in Section 2.3 has been applied: the sample was saturated with water ( $t = 0$  to  $t = 14$  min). The gas injection started at  $t = 14$  min, and the gas inlet pressure was set to 0.55 bars. The 1D vertical profiles recorded during the dry-out (from  $t = 14$  min to  $t = 28$  min) are displayed in Figure 4.

The gas saturation during the dry-out shows the variation steps already described in previous works [4, 5]. We observe a viscous gas drainage to  $Sw_i$  (until  $t = 17$  min)

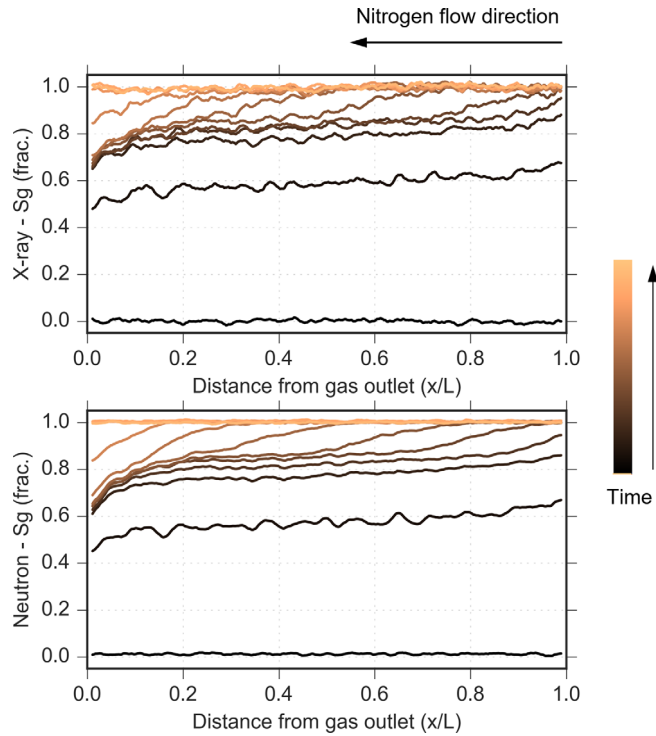


**Fig. 4.** X-ray and Neutron profiles during the dry-out with deionized water (from  $t = 14$  min to  $t = 28$  min). X-ray and Neutron beams are normalized between dry state and saturated with deionized water. Gas is injected from the right.

followed by the evaporation of the remaining trapped brine. The  $S_{wi}$  value is estimated to be 20% from these graphs. In [Figure 4](#), a front is observed during the evaporation with only a small production of water ahead of the front (the gas saturation plateau ahead of the front increase from 72% to 82% during the front advancement). Different mechanisms can explain this production ahead of the front (drainage, evaporation, or a small capillary backflow), and will be discussed later. Globally, the evaporation process is quick enough here to prevent the capillary forces from re-distribute the water in the sample.

### 3.2 Dry-out with the KBr brine

The previous experiment was reproduced with the deionized water replaced by the 100 g/L KBr brine. The same gas inlet pressure of 0.55 bars was set. The Neutron and X-ray attenuations are plotted in [Figure 5](#). In this experiment, the two attenuation curves are not superimposed due to the addition of salt. The quantity of salt and the gas saturation is computed in blue and green using the method detailed in [Appendix A.1](#) Dual modality *in-situ* monitoring. For all graphs, the quantity of salt is computed at the core scale (0.31 cc) when the total accumulation is plotted, and the pixel scale ( $6.67 \times 10^{-4}$  cc) when accumulation profiles are plotted. Before injecting the gas, the deionized water was replaced by the KBr brine. The gas injection, in the core saturated with the KBr brine, starts at  $t = 65.5$  min.

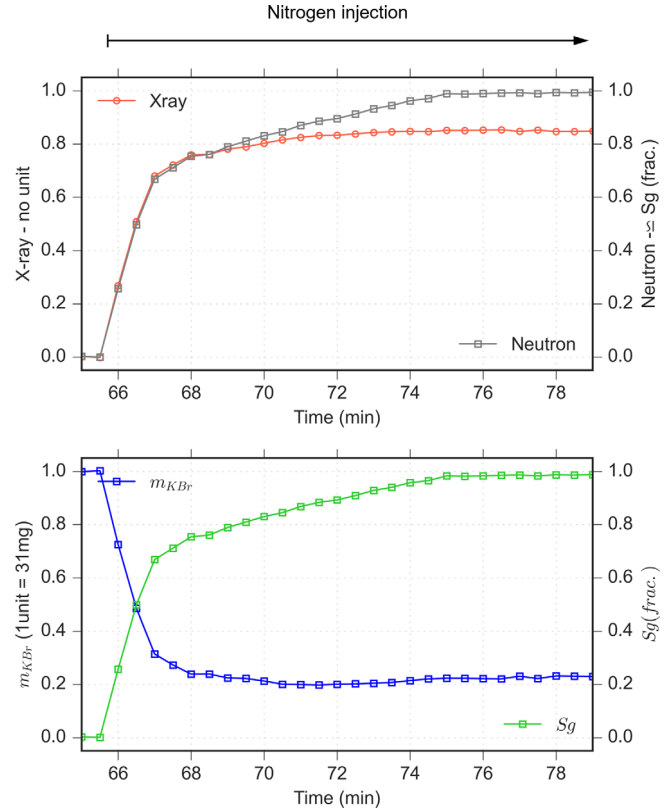


**Fig. 5.** Dry-out with the 100 g/L KBr brine. The gas is injected into the core previously saturated with the KBr brine. The mass of salt is given for a pixel volume of 0.31 cc.

The salt mass curve shows an increase from 0 to 1 unit during the replacement of deionized water by the KBr brine. Here, 1 unit is defined as 31 mg, the quantity of salt contained in a PV of  $C_0$  brine. This normalization allows for reading the fraction of the initial quantity of salt that remained trapped in the sample during the dry-out. The dry-out dynamic is similar to the previous experiment, exhibiting the same steps: (1) the viscous drainage during which the salt is produced with the water and (2) the water evaporation during which salt is left in the sample. The second step is detected when the Neutron and X-ray attenuations divert. The quantity of salt left in the core at the end of the dry-out allows the quantification of the contribution of the two production mechanisms (drainage and evaporation) to water production. Here, we observe that 20% of the initial salt remains in the sample at the end of the experiment (*cf.* blue curve on [Fig. 5](#)). This agrees with the  $S_{wi}$  value that was estimated at the end of the drainage with deionized water.

The 2D projections recorded at the end of the dry-out are given in [Figure 6](#). They clearly show a small horizontal salt bank on the X-ray projection, close to the gas outlet. The salt distribution profiles recorded at  $S_{wi}$  (dissolved in the brine) and at the end of the dry-out (precipitated in the sample) are compared in [Figure 7](#). The dissolved salt distribution shows that the capillary end-effect locally increases the quantity of salt. The edges of the sample

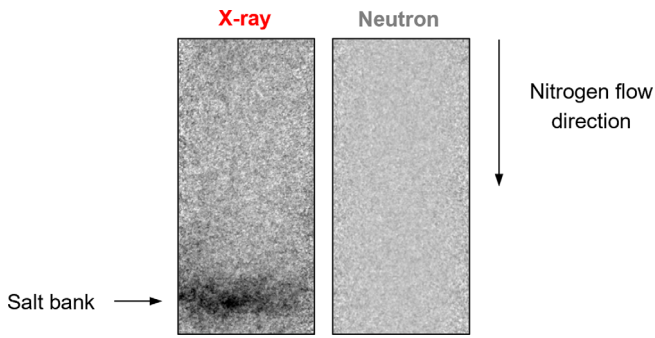


**Fig. 6.** 2D projections at the end of the dry-out (no capillary contact), when initially saturated with the KBr brine. On the X-ray projection, darker shades suggest a salt bank position. The Neutron projection shows a flat profile confirming that the sample is dry.

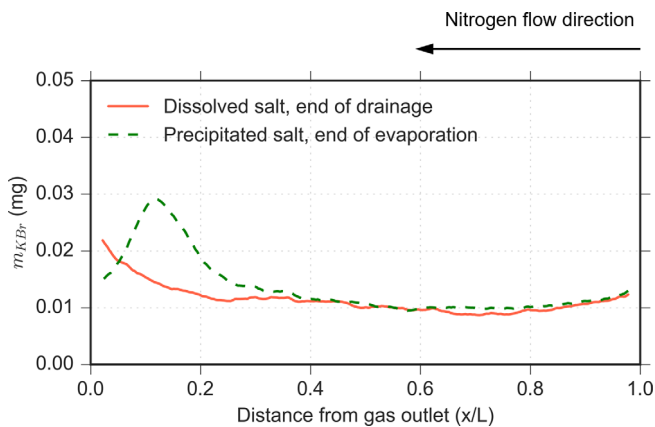


**Fig. 7.** Salt distribution, dissolved in the brine at  $Sw_i$  (plain curve) and precipitated at the end of the dry-out (dashed curve). The mass of salt is given for a pixel volume of  $6.67 \times 10^{-4}$  cc.

(1 mm from each side) are cropped during the data processing. This hides the extent of the end effect and the dissolved salt it contains. The precipitated salt curve shows a salt deposition all along the core, with an accumulation close to the outlet. It is partly explained by the initial dissolved salt distribution at  $Sw_i$  and probably also by a small redistribution of the salt contained in the capillary end-effect. However, if we exclude the capillary end-effect zone, the two curves show a perfect superposition, suggesting no water reorganization during the evaporation. The water production that was observed ahead of the front during the first experiment can therefore be explained by early evaporation. All other production mechanisms (drainage or capillary backflow) would have redistributed the salt.

### 3.3 Dry-out with capillary contact

The dry-out with the KBr brine was reproduced with a capillary contact maintained at the gas outlet using the bottom inlet and outlet lines (see Fig. 1). A recent work [4] has suggested that the capillary contact acts as a salt pump, allowing to accumulate more salt in the sample than initially dissolved. The underlying mechanism is believed to

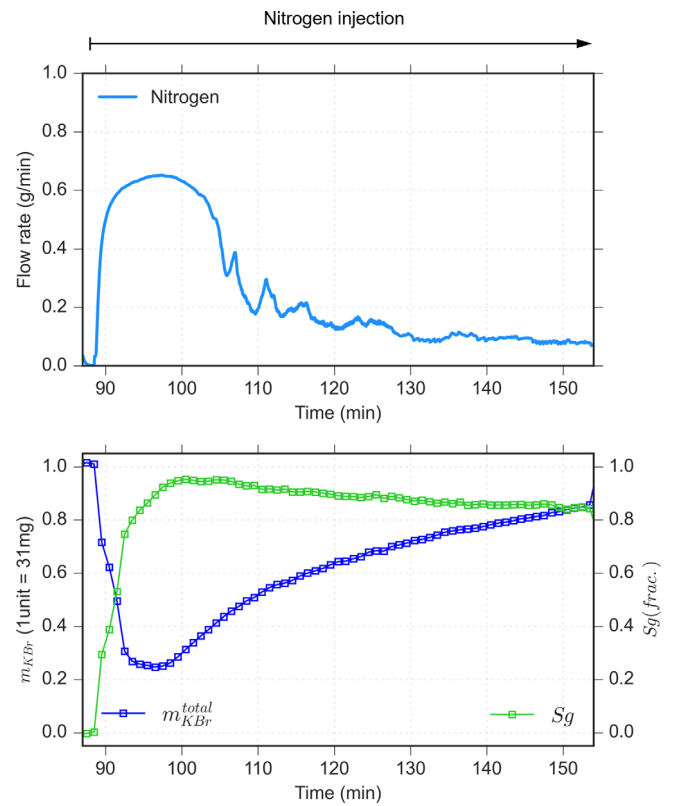


**Fig. 8.** Dry-out with the 100 g/L KBr brine and a capillary contact maintained at the gas outlet (high-pressure gradient case). The mass of salt is given for a pore volume of 0.31 cc.

be a competition between evaporation and capillary forces [4]. The effect of the gas flow rate on this equilibrium is studied: the experiment was conducted twice with the inlet pressure set to 0.55 bars and 0.35 bars. These two configurations are referred to as high- and low-pressure gradient dry-out, respectively.

#### 3.3.1 High-pressure gradient

For this dry-out experiment, the inlet gas pressure was set to 0.55 bars. The gas was injected into the sample initially saturated with the 100 g/L KBr brine. The gas flow rate during the dry-out is given in Figure 8, with the gas saturation in green and the computed salt quantity in blue.

The initial steps of the dry-out exhibit similar behaviour to the one seen previously (*i.e.*, a drainage step followed by the evaporation step). The  $Sw_i$  value can be estimated to be 20%, of the minimum salt quantity trapped after the drainage ( $t = 95$  min, blue curve). After that, the quantity of salt is multiplied by 4, from 0.2 units to 0.8 units (corresponding to 25 mg). This demonstrates a substantial salt accumulation in the sample, while only gas is injected through it. During this salt accumulation sequence, we observe a strong decrease in the gas flow rate. This is easily explained by a reduction of the initial sample permeability as salt precipitates in the porous space [4, 5]. The reduction of porosity caused by salt deposition will be estimated using the Neutron and X-ray profiles.

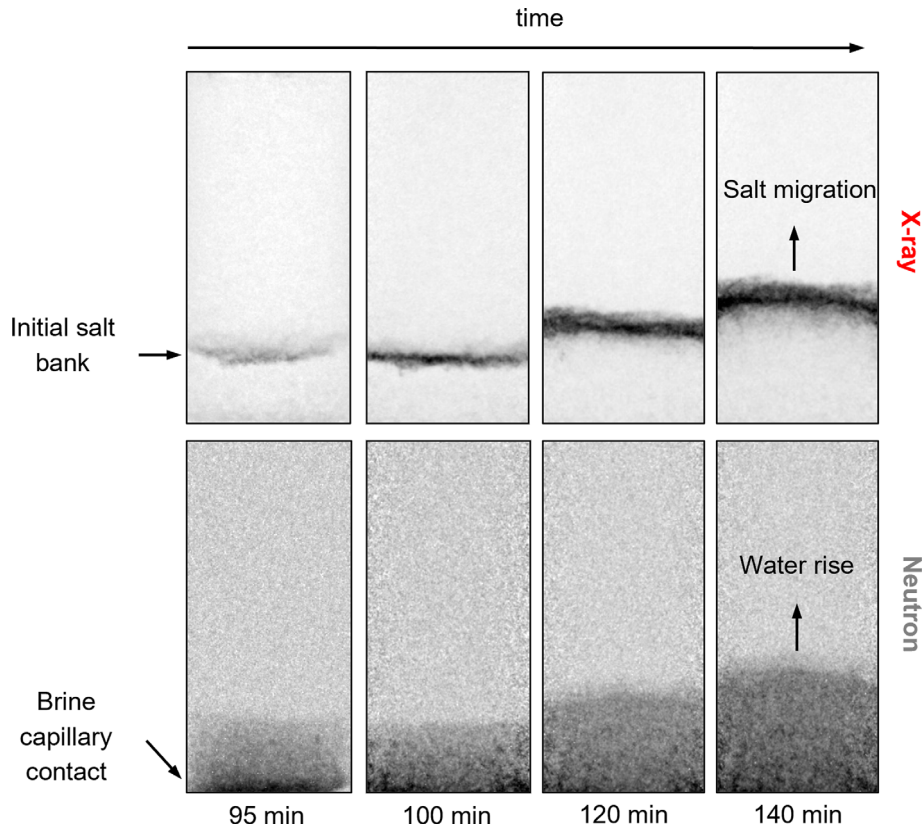


**Fig. 9.** 2D projections during the salt accumulation. Gas is injected from the top. On the X-ray projections, darker shades suggest a salt bank position. On the Neutron projections, darker shades suggest higher water saturations.

2D projections recorded before the salt starts to accumulate are shown in Figure 9 ( $t = 95$  min). They show a comparable small salt bank formed close to the gas outlet, as observed when no capillary contact was maintained (Fig. 6). However, in this experiment, the Neutron projection clearly shows that the bottom of the sample remains partially saturated with water. This behaviour is obviously due to the imposed capillary contact boundary condition.

The evolution of the initial small bank during the dry-out is shown in Figure 9. The 2D projections show a rise of both the salt bank and the water front in the sample. The evolution visible on the X-ray projections suggests an evolution in two steps: first, the salt bank is getting quickly wider and thicker while staying at the same height, and secondly, from  $t = 107$  min, it starts migrating upward in the core while slowly getting wider. During the first step, salt accumulation results in substantial gas flow rate reduction (almost 50%). Afterwards, we observe a stick and slip-like behaviour of water and salt rises.

The brine saturation  $S_w$ , the brine concentration  $C_{\text{KBr}}$  and the precipitated salt  $m_{\text{KBr}}^{\text{solid}}$  profiles are given in Figure 10 for different time steps during the salt accumulation. The profiles give meaningful insight to understand the mechanism of salt accumulation and rising. In this work, we consider that salt precipitates instantaneously once the solubility limit of  $6.5 \times C_0$  is reached excluding any super-saturation condition. The salt only precipitates when

two conditions are met:  $S_w > 0$  and  $C_{\text{KBr}} = 6.5 \times C_0$ . The brine saturation and the KBr concentration profiles show that the capillary contact maintains almost constant boundary conditions at the gas outlet which prevents salt precipitation at the outlet. The brine concentration, however, quickly rises to its limit of solubility ( $6.5 \times C_0$ ) at a few mm from the gas inlet, where salt starts to precipitate. The brine saturation profiles show that the sample is completely dry behind the salt bank. A residual value can be read on these curves, around 2%. It can be attributed to the X-ray and Neutron signals calibration. The precipitated salt curves clearly show the salt bank migration toward the gas inlet and its thickening during its displacement. Following the previous remarks, the salt migration can be explained by the waterfront displacement that carries more salt and allows the salt to precipitate higher in the sample.

The reduction of porosity is computed from the precipitated salt curves (*cf.* Eq. (A6)) and it is directly proportional to the precipitated salt quantity. The apparent migration of the salt starts when the local porosity is reduced by up to approximately 12–14% in some sections of the sample. At the end of the experiment (at  $t = 155$  min), some sections of the sample show a reduction of the pore space by up to 20%. This relatively moderate porosity reduction induces an average flow rate reduction by almost a ratio of 6 (*cf.* maximum to minimum ratio of flow rate in Fig. 8). This observation supports the hypothesis of preferential salt

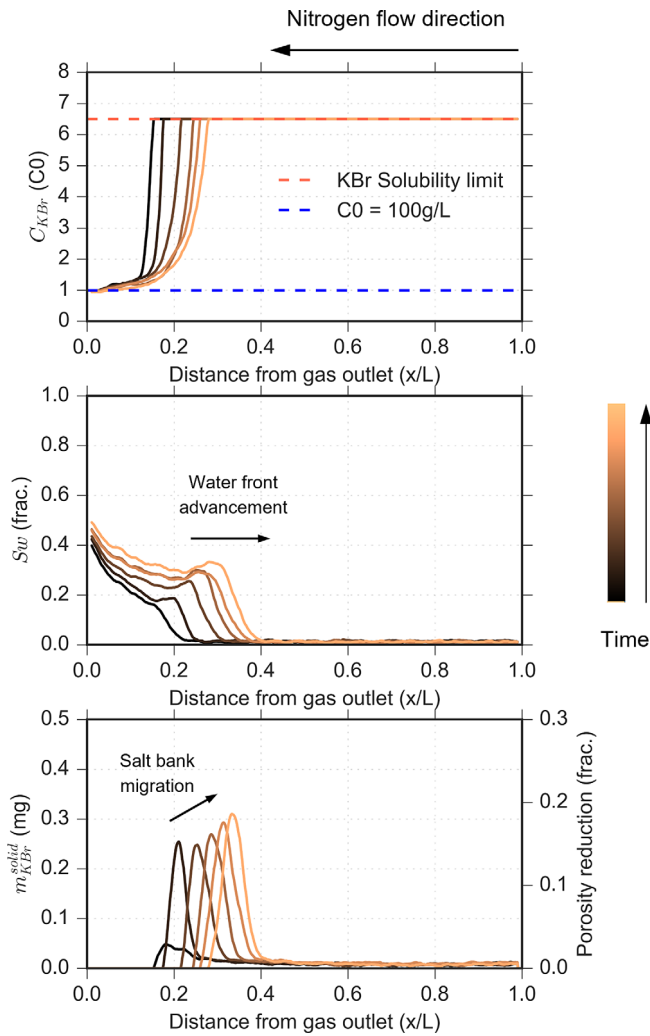


**Fig. 10.** Brine concentration  $C_{KBr}$ , brine saturation  $S_w$  and precipitated salt profiles  $m_{KBr}^{solid}$  computed during the salt accumulation. The reduction of porosity is estimated from the  $m_{KBr}^{solid}$  curves. Profiles are computed regularly from  $t = 100$  min to  $t = 150$  min. The mass of salt is given for a pixel volume of  $6.67 \times 10^{-4}$  cc.

precipitation along the pore wall plugging by the throats between pores.

These different curves are plotted for a single time step on the same plot in Figure 11. It shows the relation between the salt bank and the brine phase. The section where salt precipitates are saturated by both the gas and the brine. The presence of these two phases is required to allow precipitation. The salt bank does not act as a barrier for the brine. It is in a constant rise in the sample by capillary forces, but the height reached by the front is limited by its evaporation. If deionized water had been used, the height reached would have quickly stabilized. Here, the evaporation is causing salt to precipitate. As it accumulates in the pore space, the porosity is reduced and the gas flow rate decreases (Fig. 8), changing the equilibrium between capillary forces and evaporation speed. The decrease in the gas flow rate allows the water to imbibe higher in the sample. Salt

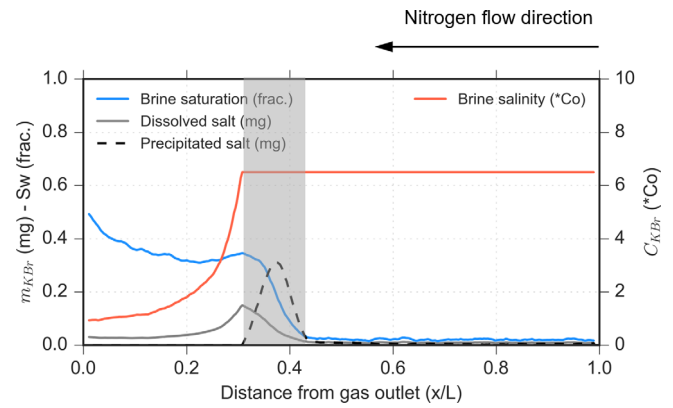


**Fig. 11.** Salt repartition in the different phases during the dry-out with capillary contact ( $t = 150$  min). The grey area shows where the conditions for salt precipitation are met. The mass of salt is given for a pixel volume of  $6.67 \times 10^{-4}$  cc.

precipitates ahead of the previous bank while its rear back is dissolved by under-saturated brine.

The curves plotted in Figure 11 show the equilibrium of the different phases for specific injection conditions. The brine phase is not breaking through the sample, suggesting flowing conditions close to null. From  $t = 100$  min to  $t = 150$  min, the water saturation is increased by 9% by capillary rise, corresponding to an average flow rate of  $33 \mu\text{L/h}$ . Yet, this flow rate is not high enough to explain the rate of salt accumulation in the sample. Indeed, the brine is constantly evaporating in the gas, and it is compensated by an additional brine pumping through the capillary contact. This additional contribution is estimated using the salt mass curve to an average of  $190 \mu\text{L/h}$  between  $t = 95$  min to  $t = 150$  min. It is twice more important during the early stages of the dry-out. Despite the brine saturation profiles being close to static, the brine flow rate is far from null. It explains how the rear back of the salt bank is quickly dissolved while the brine slowly rises.

### 3.3.2 Low-pressure gradient

For the second dry-out experiment with capillary contact, the inlet gas pressure was set to 0.35 bars. The gas was injected into the sample initially saturated with the  $100 \text{ g/L}$  KBr brine. The gas flow rate during the dry-out is given in Figure 12, with the gas saturation in green and the salt quantity in blue.

The early phases of the dry-out are again comparable to what has been reported previously. The initial salt bank is formed halfway up the sample, higher than in the previous experiment. This is consistent with the lower inlet pressure allowing the capillary forces and the brine evaporation to equilibrate higher in the sample.

The next steps of the dry-out demonstrate a completely different behaviour than the one previously observed, with the gas flow rate showing alternating phases of draw-down and build-up (see phases referred to as 1 and 2 in Fig. 12). The gas saturation is correlated to these variations: the higher the gas flow rate, the higher the gas saturation. During the draw-down phases, the gas flow rate is reduced to a

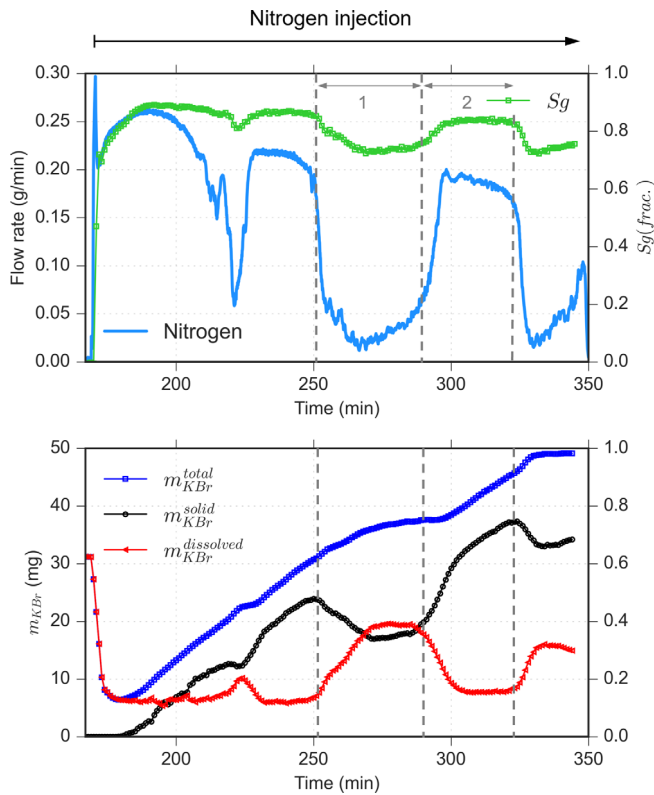


**Fig. 12.** Dry-out with the 100 g/L KBr brine and a capillary contact maintained at the gas outlet (low-pressure gradient case). The two sections noted 1 and 2 show a cycle of gas draw-down and gas build-up. The mass of salt is given for a pore volume of 0.31 cc.

tenth of its initial value (from 0.25 g/min to 0.025 g/min), while the total quantity of salt in the sample is increasing monotonously. The quantity of salt dissolved in the brine and the quantity of salt precipitated in the sample are also displayed in Figure 12 in red and black respectively. These two curves demonstrate the same alternating cycles of build-up and draw-down, yet inversely correlated. Indeed, during a gas draw-down, the quantity of precipitated salt decreases while the quantity of dissolved salt in the brine phase increases, and conversely during a gas build-up. These curves suggest the phases of gas draw-down and build-up are controlled by cycles of salt precipitation and salt dissolution.

The 2D X-ray projections recorded during the draw-down and build-up phases are given respectively in Figure 13. The corresponding precipitated salt profiles computed for different time steps are given in Figure 14, for the draw-down and the build-up.

As seen earlier, the gas draw-down is initiated by a strong reduction of the porosity in a limited section of the core. For the draw-down described here, the porosity is reduced by up to 24%, see Figure 14a. This allows first the rinsing of the brine in the sample while dissolving the rear back of the salt bank and then the precipitation of the salt higher in the sample. These steps are clearly visible on the 2D X-ray projections, Figure 13. The quantity of salt

dissolved is balanced by the quantity of salt that precipitates. The total quantity of salt is still showing an increase due to the rise of the water in the sample, pumping additional dissolved salt through the capillary contact. The major difference with the previous dry-out experiment is that a second salt bank is formed here, while a unique one was observed previously. This difference is crucial as it triggers the gas build-up cycle: the formation of a second salt bank globally spreads the salt in a less damaging configuration for permeability. This is well understood in Figure 14a: the maximum porosity reduction falls from 24% to 16% during the formation of the second bank. The gas flow rate quickly increases following this, initiating the gas build-up.

During the gas build-up, the water is withdrawn from the sample, and no salt dissolution is observed. The newly formed salt bank is left ahead of the waterfront, where the sample is dry and only salt precipitation is observed during this phase. This is clearly visible on the salt profiles in Figure 14b and on the 2D projections given in Figure 13. It is during these phases of gas build-up that the quantity of salt in the sample increases the most. The porosity is strongly reduced again during this step and consequently triggers the next gas draw-down phase.

Results of a similar experiment have been published in [4], using a comparable rock sample (a Bentheimer plug) and identical fluids (dry Nitrogen and a 100 g/L KBr brine). In their experiment the imposed pressure gradient is 0.150 bars, leading to lower gas injection flow rates. The experiment was monitored using X-Ray only, limiting the possibility to compute the gas saturation or to quantify the salt accumulation [18]. They overcome the experimental limitation using numerical simulations (more information on the numerical model is given in [19]), providing results of salt accumulations (both dissolved and precipitated) and fluid saturations. These simulation results are shown in Figure 18. The original data (Fig. 18 from [4]) have been modified to match the units used in Figure 12. Their work offers the opportunity to compare simulated results of salt accumulation with the experimental ones that have been computed using the dual-modality imaging. The comparison shows great similarities in salt accumulation: the increase in total salt accumulation is mainly due to an accumulation of precipitated salt. The quantity of salt dissolved in the brine phase remains low, mostly driven by the gas saturation. The major difference is the amplitude of the salt transfer from dissolved to precipitated (and *vice versa*) during the phases of gas build-up and draw-down, the latter is observed to a lesser extent in the simulation results (Fig. 18) than in the experimental results (Fig. 12). These salt transfers explained how the salt bank could migrate along the core, and eventually split into several salt banks. This difference can either find an experimental or a numerical explanation. For the experimental one: the results of this work have shown that a different behaviour of salt accumulation was observed for different flowing conditions (referred to here as the high- and the low-pressure gradient). The lower pressure gradient used in the compared study [4] might have led to the different behaviour of salt transport in the core. For the numerical explanation: the

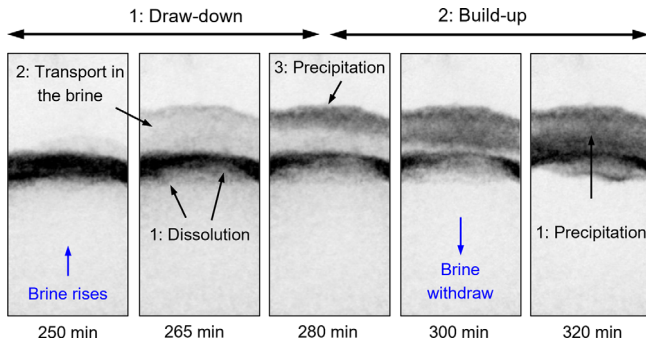


**Fig. 13.** 2D X-ray projections during (1) a gas draw-down (see cycle 1 in Fig. 12), and (2) a gas build-up (see cycle 2 in Fig. 12). Gas is injected from the top. Darker shades suggest salt bank position.

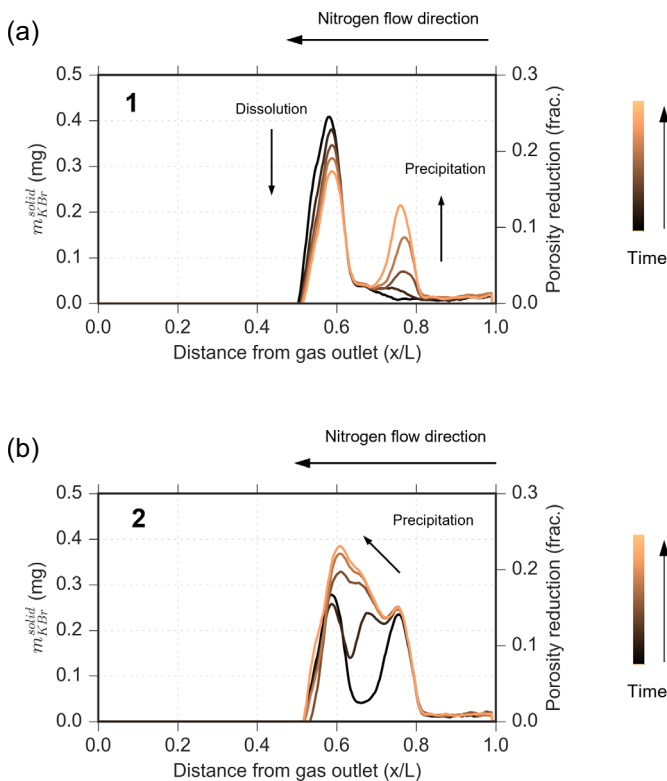


**Fig. 14.** Precipitated salt profiles during (a) a gas draw-down (see cycle 1 in Fig. 12) and (b) a gas build-up (see cycle 2 in Fig. 12). The mass of salt is given for a pixel volume of  $6.67 \times 10^{-4}$  cc.

thermodynamic model assumes an instantaneous fluids equilibrium while it might more likely have an equilibration kinetic (especially for the brine evaporation). An equilibration kinetic could delay the salt precipitation, increasing the quantity of salt dissolved in the brine.

The simulated salt accumulation can also be compared at the local scale. Their simulation (Fig. 19 of [4]) shows that the gas draw down is triggered by local salt accumulations of 1.1–1.2 mg, corresponding to local porosity

reduction of 60% to 65% (salt mass is computed with additional information provided by the authors, and converted for a volume of  $6.67 \times 10^{-4}$  cc). These simulated values of local porosity reductions are more than twice what has been estimated here. The explanation remains uncertain but a comparison of their salt profiles along the core (Fig. 19 of [4]) shows that the simulation leads to a thinner salt bank than what has been observed in this study. The previous comparison showed that the total accumulation of solid salt was comparable between the simulation and the experimental data. Yet its repartition and spread in the salt bank are different. This observation is crucial as their simulation has been used to history match a model of permeability alteration as a function of the porosity reduction. An erroneous simulation of the salt bank will lead to an erroneous calibration of the permeability alteration model.

## 4 Conclusion

The dual-modality monitoring technique has demonstrated a real contribution to the study of the salt precipitation dynamic induced by gas flow-through drying. The difference in attenuation pattern between the Neutron and the X-ray beams is used to de-correlate beam attenuations caused by the water and the salt. A method to calibrate and process the two signals has been presented, allowing the separate quantification of the different phase saturations and brine salinity as well as the reduction of porosity caused by the salt deposition. This information is crucial to better calibrate numerical models and particularly the permeability reduction with salt precipitation.

The results of four dry-out experiments monitored with this method are presented here. The two first experiments mostly aimed to calibrate the dual modalities for the different phases. The last two experiments have been conducted with a brine capillary contact maintained at the gas outlet. Experimental data have given new insight into the organization of the three phases (the brine, the gas and the precipitated salt) when a salt bank is formed in the sample. The quantity of salt that accumulates allows the estimation of the flow rate of brine pumped through the capillary contact to compensate for the brine evaporation in the gas phase. The observations have shown that a reduction of the initial porosity in some sections of the sample by 12–14% was enough to trigger a gas draw-down, characterized by the migration of the salt toward the gas inlet. The rise of the salt bank involves three steps: salt dissolution, salt transport in the brine phase and salt precipitation where the waterfront stabilizes. In some conditions (low gas pressure gradient for example), the rise of the water can be fast enough to form a second salt bank higher in the sample. It has been observed that the formation of the second salt bank could spread the precipitated salt in a less damaging configuration for the gas flow, triggering a phase of gas build-up characterized by the withdrawal of the water. These phases of gas draw-down and build-up can alternate until the sample clogging.

Finally, these quantities computed using dual-modality imaging (gas saturation and salt accumulations) show great

similarities with simulations of salt precipitation presented in published work. Yet, some differences could also be observed: the simulation seems to lead to thinner salt banks than experimentally observed, characterized by higher concentrations of precipitated salt. This observation is valuable as the precipitated salt concentration determines the local reduction of porosity, on which the injectivity impairment models generally rely.

Future works can include:

- The construction of a permeability reduction curve as a function of the porosity reduction.
- The evaluation of the thermodynamic aspect of the drying, especially the water vapour concentrations.

## Funding information

The NeXT-Grenoble project was supported by the French National Research Agency in the framework of the “Investissements d’avenir” program (ANR-15-IDEX-02).

## Data availability

DOI of the neutron data: [10.5291/ILL-DATA.UGA-77](https://doi.org/10.5291/ILL-DATA.UGA-77).

## References

- 1 Kleinitz W., Dietzsch G., Köhler M. (2003) Halite scale formation in gas-producing wells, *Chem. Eng. Res. Des.* **81**, 3, 352–358. <https://doi.org/10.1205/02638760360596900>.
- 2 Whitaker S. (1977) Simultaneous heat, mass, and momentum transfer in porous media: a theory of drying, in *Advances in Heat Transfer*, J.P. Hartnett, T.F. Irvine (eds.), Elsevier, pp. 119–203 [Online]. Available: <https://www.sciencedirect.com/science/article/pii/S0065271708702235>.
- 3 Prat M., Bouleux F. (1999) Drying of capillary porous media with a stabilized front in two dimensions, *Phys. Rev. E* **60**, 5, 5647–5656. <https://doi.org/10.1103/PhysRevE.60.5647>.
- 4 Lopez O., Youssef S., Estublier A., Alvestad J., Strandli C. W. (2020) Permeability alteration by salt precipitation: Numerical and experimental investigation using X-Ray Radiography, *E3S Web Conf.* **146**, 3001. <https://doi.org/10.1051/e3sconf/202014603001>.
- 5 Peysson Y., Bazin B., Magnier C., Kohler E., Youssef S. (2011) Permeability alteration due to salt precipitation driven by drying in the context of CO<sub>2</sub> injection, *Energy Proc.* **4**, 4387–4394. <https://doi.org/10.1016/j.egypro.2011.02.391>.
- 6 Peysson Y., André L., Azaroual M. (2014) Well injectivity during CO<sub>2</sub> storage operations in deep saline aquifers – Part 1: Experimental investigation of drying effects, salt precipitation and capillary forces, *Int. J. Greenh. Gas Control.* **22**, 291–300. <https://doi.org/10.1016/j.ijggc.2013.10.031>.
- 7 Aquilina P. (2012) Impairment of gas well productivity by salt plugging: a review of mechanisms, modeling, monitoring methods, and remediation techniques, in: *Paper presented at the SPE Annual Technical Conference and Exhibition, San Antonio, Texas, USA, October 2012*. SPE-158480-MS.
- 8 André L., Peysson Y., Azaroual M. (2014) Well injectivity during CO<sub>2</sub> storage operations in deep saline aquifers – Part 2: Numerical simulations of drying, salt deposit mechanisms and role of capillary forces, *Int. J. Greenh. Gas Control.* **22**, 301–312. <https://doi.org/10.1016/j.ijggc.2013.10.030>.
- 9 Giorgis T., Carpita M., Battistelli A. (2007) 2D modeling of salt precipitation during the injection of dry CO<sub>2</sub> in a depleted gas reservoir, *Energy Convers. Manag.* **48**, 6, 1816–1826. <https://doi.org/10.1016/j.enconman.2007.01.012>.
- 10 Mahadevan J., Sharma M.M., Yortsos Y.C. (2006) Flow-through drying of porous media, *AIChE J.* **52**, 7, 2367–2380. <https://doi.org/10.1002/aic.10859>.
- 11 Figus C., Bray Y., Bories S., Prat M. (1999) Heat and mass transfer with phase change in a porous structure partially heated: continuum model and pore network simulations, *Int. J. Heat Mass Transf.* **42**, 14, 2557–2569. [https://doi.org/10.1016/S0017-9310\(98\)00342-1](https://doi.org/10.1016/S0017-9310(98)00342-1).
- 12 Plourde F., Prat M. (2003) Pore network simulations of drying of capillary porous media. Influence of thermal gradients, *International Journal of Heat and Mass Transfer* **46**, 1293–1307. [https://doi.org/10.1016/S0017-9310\(02\)00391-5](https://doi.org/10.1016/S0017-9310(02)00391-5).
- 13 Mahadevan J., Sharma M.M., Yortsos Y.C. (2007) Water removal from porous media by gas injection: Experiments and simulation, *Transp. Porous Media* **66**, 3, 287–309. <https://doi.org/10.1007/s11242-006-0030-z>.
- 14 Le D., Hoang H., Mahadevan J. (2009) Impact of capillary-driven liquid films on salt crystallization, *Transp. Porous Media* **80**, 2, 229. <https://doi.org/10.1007/s11242-009-9353-x>.
- 15 Tengattini A., Lenoir N., Andò E., Giroud B., Atkins D., Beaucour J., Viggiani G. (2020) NeXT-Grenoble, the Neutron and X-ray tomograph in Grenoble, *Nucl. Instrum. Methods Phys. Res. A: Accel. Spectrom. Detect. Assoc. Equip.* **968**, 163939. <https://doi.org/10.1016/j.nima.2020.163939>.
- 16 Grünauer F. (2005) Design, optimization, and implementation of the new neutron radiography facility at FRM-II, [Online]. Available: <https://pdfs.semanticscholar.org/041f/fe1ef9477759f231bd46224240ef152141d7.pdf>.
- 17 Tengattini A., Lenoir N., Andò E., Viggiani G. (2021) Neutron imaging for geomechanics: A review, *Geomech. Energy Environ.* **27**, 100206. <https://doi.org/10.1016/j.gete.2020.100206>.
- 18 Youssef S., Mascle M., Vizika O. (2018) High throughput coreflood experimentation as a tool for EOR project design, in: *SPE Improved Oil Recovery Conference, Tulsa, Oklahoma, USA*.
- 19 Gassara O., Estublier A., Garcia G., Noirez S., Cerepi A., Loisy C., Le Roux O., Petit A., Rossi L., Kennedy S., Brichtart T., Chiquet P., Luu Van Lang L., André Duboin F., Gance J., Texier B., Lavielle B., Thomas B. (2021) The aquifer-CO<sub>2</sub> leak project: Numerical modeling for the design of a CO<sub>2</sub> injection experiment in the saturated zone of the Saint-Emilion (France) site, *Int. J. Greenh. Gas Control.* **104**, 103196. <https://doi.org/10.1016/j.ijggc.2020.103196>.
- 20 Rinard P. (1991) Neutron interactions with matter, *Passive Nondestructive Assay of Nuclear Materials* 375–377.

## Appendix

### A.1 Dual modality *in-situ* monitoring

Dynamic *in-situ* monitoring was performed using the NeXT-Grenoble station recently designed at ILL [15]. It is

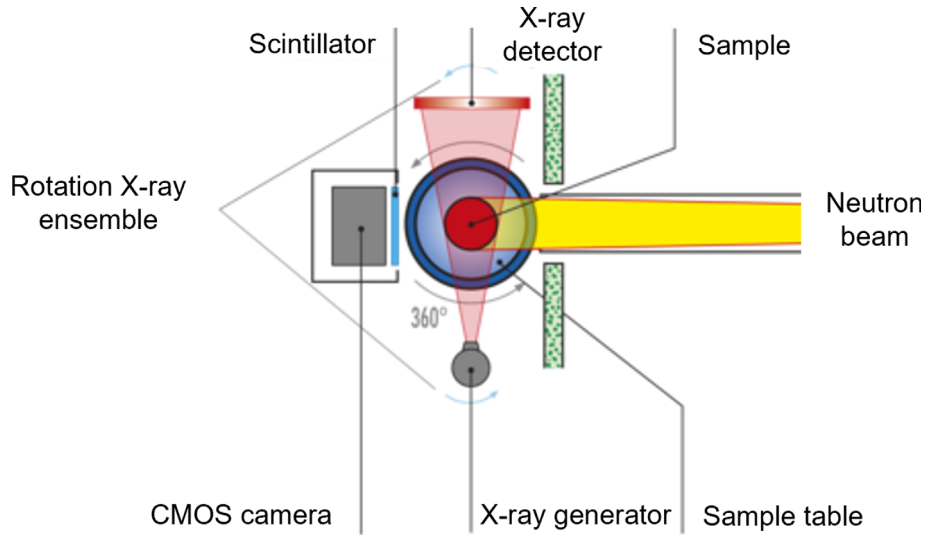


**Fig. A1.** Schematized top view of the NeXT dual modality lines (modified from [15]).

composed of dual Neutron and X-ray modalities, simultaneously monitoring the sample from a different angle (see illustration Fig. A1). A nuclear reactor supplies several experimental stations with neutron flux (hot, thermal, or cold neutrons). The NeXT station (used here) is supplied by a flux of up to  $1.4 \text{ E}10 \text{ n/cm}^2/\text{s}$  cold neutrons at the beam port. A medium-resolution detector was used here to acquire neutron radiographies. It is composed of a scintillator, a mirror and a camera plus optics. X-rays are generated using a sealed source generator (Hamamatsu L12161-07 X-ray microfocuss generator). X-rays are monitored using a VarexScan® detector, equipped with a Cesium Iodide scintillator. Within the frame of this study, a total of 42 h of beam time have been granted to run all experiments. This limit of time has constrained the quantities of an experiment that could be run, and no high-resolution computed tomography could have been acquired.

The main advantage of the dual modality is to benefit from different beam attenuation patterns [9, 15]. As hydrogen's neutron attenuation coefficient is very high compared to the other materials used here, the Neutron contrast is mainly sensitive to water saturation. X-ray contrast however is sensitive to both water saturation and salt content.

The main parameters for radiography acquisitions are an X-ray pixel resolution of  $40 \mu\text{m}$ ; Neutron pixel resolution of  $15 \mu\text{m}$ ; acquisition time of 6 s for both beams. Using this configuration, the resulting X-ray attenuation maps appear to be noisier than the Neutron ones. The 2D Neutron and X-ray projections are pre-processed to allow further quantitative computations. First, the Neutron projections are downscaled by a factor of 0.375 ( $=15 \mu\text{m}/40 \mu\text{m}$ ) to match the X-ray projection pixel resolution. Then, the Neutron and the X-ray projections are registered to have the two sets of projections spatially aligned. It should be noted that the two beams are hitting the core sample from a different angle (around  $70^\circ \text{C}$ , see Fig. A1), the sample is not rotated during the monitoring,

as it would have reduced the time resolution of the two beam acquisitions. Therefore, the two sets of projections are not showing the same 2D view of the core (especially in the radial direction). This effect is mitigated when considering the mean value (2D projection averaged on the whole sample range) or the vertical profile (2D projection averaged in the radial direction) as well as the axial symmetry of the process. Finally, the natural logarithm is applied to all projections.

For both beams, the relation between intensity attenuation and the materials crossed can be expressed using the Beer-Lambert law [20]. For a multi-component system, it can be written as (A1):

$$I(t) = I_0 e^{-\sum \mu_i x_i} \quad (\text{A1})$$

where  $I(t)$  and  $I_0$  respectively refer to the transmitted and incident ray intensity,  $\mu_i$  and  $x_i$  are respectively the attenuation coefficient and linear path of material  $i$  crossed by the beam. The summation operation  $\sum$  applies to all material crossed between the source and the detector, including all the cell components, the rock sample and the fluids saturating the rock. All constant quantities can be gathered and lumped in the incident ray intensity. In these experiments, three material paths are changing through time, namely deionized water, nitrogen, and salt. For all computations, the following simplifying hypotheses are made: (i) The KBr salt has the same attenuation coefficient when a solid or dissolved state and (ii) X-ray attenuation is linear to the salt quantity. With these hypotheses, the intensity attenuation  $I(t)$  can be expressed for both beams as follows (A2):

$$I(t) = I'_0 e^{-\sum \mu_{\text{H}_2\text{O}} x_{\text{H}_2\text{O}} + \mu_{\text{KBr}} x_{\text{KBr}} + \mu_{\text{N}_2} x_{\text{N}_2}} \quad (\text{A2})$$

$$\text{with } I'_0 = I_0 e^{-\alpha}$$

where  $\alpha$  accounts for the constant contribution to the beam attenuation of the set-up. The conservation of the

total length path  $X$  of material crossed allows us to write equation (A3):

$$x_{\text{H}_2\text{O}} + x_{\text{N}_2} + x_{\text{KBr}} = X. \quad (\text{A3})$$

As the natural logarithm is applied to all projections during the pre-processing, equation (A2) becomes:

$$\log[I(t)] = \log[I'_0] - \sum_{\text{N}_2, \text{H}_2\text{O}, \text{KBr}} \mu_i x_i. \quad (\text{A4})$$

Equation (A4) needs to be calibrated for each modality to characterize the attenuation coefficients of all materials. This can be easily performed for  $\mu_{\text{H}_2\text{O}}$  and  $\mu_{\text{N}_2}$  by saturating the sample with deionized water and nitrogen. However, the salt coefficient  $\mu_{\text{KBr}}$  cannot be directly measured using its pure phase (solid salt), but its contribution to the Neutron and X-ray intensities attenuations can be estimated using a mixture: the 100 g/L KBr brine (referred to as the  $C_0$  brine). This solution allows calibrating the attenuations for a pore volume filled with 31 mg of KBr salt ( $C_0 \times \text{PV}$ ) and the remaining space by deionized water ( $\mu_{\text{C}_0} \times X = x_{\text{KBr}} \times \mu_{\text{KBr}} + \mu_{\text{H}_2\text{O}} \times x_{\text{H}_2\text{O}}$ , with  $x_{\text{KBr}} + x_{\text{H}_2\text{O}} = X$ ). Its comparison to the Neutron and X-ray values recorded with the deionized water will determine the contribution of the salt alone.

The calibration of both beams was conducted with the following injection sequence:

1. The sample was initially dried and saturated with  $\text{N}_2$ .
2. It was saturated with deionized water (see details in Sect. 2.3)
3. It was then saturated with the  $C_0$  brine using miscible displacement.
4. Nitrogen was injected into the brine. Only the first steps were recorded during the viscous drainage, before the water evaporation starts, changing the brine concentration.

The mean Neutron and X-ray intensities monitored during the calibration are displayed in Figure A2. The two signals' variations are normalized between the dry state ( $\text{N}_2$  saturated, reached at the end of step 1) and saturated with the  $C_0$  brine ( $C_0$  saturated, reached at the end of step 3). Equation (A4) can be written for both beams for these two chosen references, giving respectively:

$$\log[I(\text{N}_2)] = \log[I'_0] - \mu_{\text{N}_2} X \quad (\text{when } \text{N}_2 \text{ saturated})$$

$$\log[I(\text{KBr})] = \log[I'_0] - \mu_{\text{C}_0} X \quad (\text{when } C_0 \text{ saturated})$$

with the normalization, equation (A4) becomes:

$$\frac{\log[I(t)] - \log[I(C_0)]}{\log[I(\text{N}_2)] - \log[I(C_0)]} = \frac{\mu_{\text{C}_0} X - \sum_{\text{N}_2, \text{H}_2\text{O}, \text{KBr}} \mu_i x_i}{X(\mu_{\text{C}_0} - \mu_{\text{N}_2})}. \quad (\text{A5})$$

All projections (Neutron and X-ray) are processed with the operations described by equation (A5). The equations are applied at the voxel scale. When computing average values (such as the gas saturation or the salt quantities), the

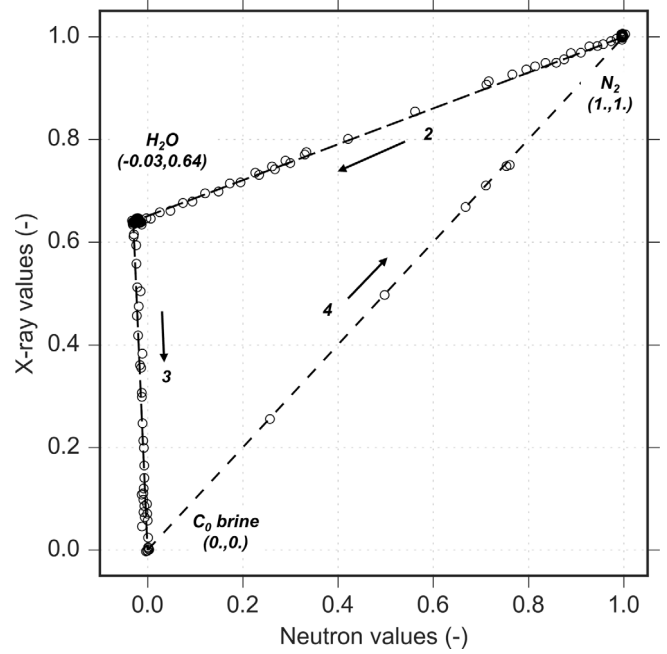


**Fig. A2.** Scatter plot of X-ray and Neutron values during the calibration experiment. Arrows indicate the injection sequences described in the text. X-ray and Neutron values are obtained with equation (A5).

averaging process accounts for the cylindrical shape of the plug, through weighting coefficients, defined at the voxel scale. The latter are computed considering a homogeneous cylindrical shape for the core. The values obtained after this processing are no longer intensity attenuation maps. They do not express a saturation either, as the sample saturation evolves between more than two phases. They are referred to as the X-ray and the Neutron values in the rest of the text. In this system of normalization, the X-ray and the Neutron values are both set to 0 when the sample is saturated with  $C_0$  brine ( $x_{\text{C}_0} = X$ ); and to 1 when it is dry ( $x_{\text{N}_2} = X$ ). The question that remains is how these values behave when the brine salinity is changed (lower or higher salinities).

The normalization described above is used for all ensuing representations. The cross-plot (Fig. A2) shows the Neutron and X-ray values for our three reference phases: the nitrogen, the deionized water and the  $C_0$  brine. Their coordinates (in this system of normalization) are given on the plot. All the points between these poles are recorded during the phased replacement. They show a perfect linear evolution from pole to pole. The positions of the poles confirm that the Neutron attenuation is mainly sensitive to water (because of the hydrogen). However, there is a small variation between deionized water and  $C_0$  brine:  $C_0$  brine attenuates slightly less the Neutron than the deionized water. It might be explained by the effect of dilution of the water molecules by the ionic species dissolved in the brine. For the X-ray, both the salt and the water attenuate the beam: the attenuation measured between the  $\text{N}_2$  phase, and the  $C_0$  phase is caused at 36% by the water molecules and at 64% by the dissolved salt.

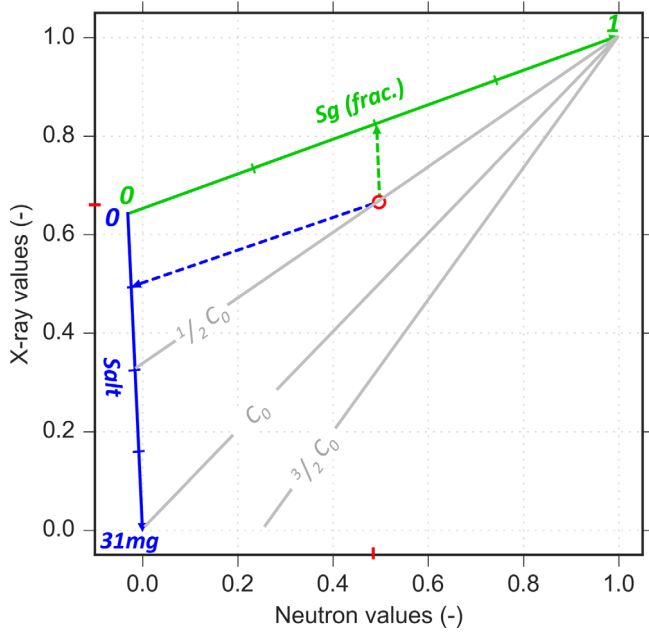


**Fig. A3.** Illustration of gas saturation, salt quantity and brine concentration computations from Neutron and X-ray measurements (red marker). Explanations are given in the text.

These poles and vectors that connect them draw a two-axis plot that enables the computation of the gas saturation  $Sg$ , the salt quantity  $m_{KBr}$  and the brine concentration  $C_{KBr}$  from the Neutron and X-ray values. These axes are drawn in Figure A3. The green axis expresses the gas saturation, and the blue axis expresses the salt quantity (1 unit = 31 mg, the quantity of salt contained in one PV of  $C_0$  brine). The grey diagonals give the brine concentration, in the  $C_0$  unit. An example is given in Figure A3 with a Neutron and X-ray measurement (see the red marker) that records the saturation process, halfway through, of the dry sample with a 50 g/L KBr brine ( $C_0/2$  brine). The marker projection on the saturation axis gives the gas saturation:  $Sg = 0.5$ ; its projection on the salt axis gives the quantity of salt:  $\frac{1}{4} \times 31 \text{ mg} = 0.8 \text{ mg}$ ; and the grey diagonal the marker falls on gives the brine concentration:  $C_0/2$ .

The previous calculus strictly applies only when all the salt is dissolved in the brine phase. A correction is made when salt precipitates. Its effect on X-ray attenuation is

considered to be the same, following the hypothesis made above, but its effect on Neutron attenuation is different. When the salt is dissolved in the brine phase, it alters the density of water and causes the reduction of attenuation described above. When the salt is in the solid state, a third phase is formed. It still attenuates the X-ray, but no longer alters the brine phase (and no longer affects the Neutron). The volume it occupies is computed using a salt density of 2.75 g/cc. The reduction of porosity caused by the salt precipitation could then be estimated using equation (A6):

$$\phi = \frac{m_{KBr}^{solid}}{\rho_{KBr} * PV} \quad (A6)$$

## A.2 Additional materials

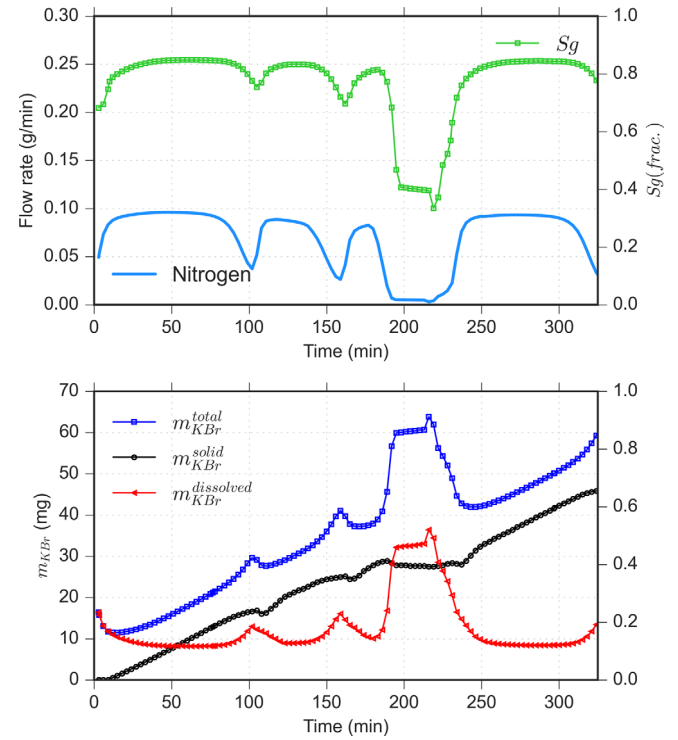


**Fig. A4.** Published data [4]: Simulated gas saturation, gas flow rate, and BKR salt accumulation (total, solid and dissolved) during gas dry-through experiments (modified graph from figure 18 of [4]). The mass of salt is given for a pore volume of 0.31 cc.